Potential Vorticity Dynamics of Tropical Instability Vortices

Journal of Physical Oceanography, 2014, 44 (3), 995–1011

R. Holmes, L. Thomas, L. Thompson and D. Darr

Potential Vorticity Dynamics of Tropical Instability Vortices

RYAN M. HOLMES AND LEIF N. THOMAS

Environmental Earth System Science, Stanford University, Stanford, California

LUANNE THOMPSON AND DAVID DARR

School of Oceanography, University of Washington, Seattle, Washington

(Manuscript received 8 July 2013, in final form 10 October 2013)

ABSTRACT

Tropical instability vortices (TIVs) in the equatorial Pacific exhibit energetic horizontal and vertical circulation characterized by regions of high Rossby number and low Richardson number. Their strong anticyclonic vorticity and vertical shear can influence the broader-scale circulation by driving lateral mixing and vertical exchange between the ocean surface and interior. The authors use a set of nested high-resolution simulations of the equatorial Pacific, with a finest grid size of 3 km, to examine the vortex dynamics associated with TIV core water formation. TIV cores are characterized by low values of the Ertel potential vorticity (PV) as the relative vorticity is anticyclonic with magnitude comparable to the local Coriolis parameter. A study of the variation of PV and other scalars along Lagrangian fluid parcel tracks entering the TIVs shows that the low-PV water in their cores is a mix of Equatorial Undercurrent (EUC) water and North Equatorial Counter Current (NECC) water. The EUC water is characterized by strong horizontal vorticity, and thus, the baroclinic component of the PV is nonnegligible and acts as a source for the anticyclonic vorticity of TIVs. This horizontal vorticity is tilted by an ageostrophic secondary circulation associated with strain-induced frontogenesis that tends to form along the path of the EUC water that enters the vortex. Frontogenesis disrupts the cyclogeostrophic balance of the frontal flow and drives differential vertical motions across the front. These results emphasize the role of submesoscale physics in the equatorial region, which are active when both the Rossby and Richardson numbers are $O(1)$.

1. Introduction

The mean circulation in the upper equatorial Pacific comprises a series of alternating zonal jets and north and south equatorial temperature fronts on either side of the eastern Pacific cold tongue (Johnson and McPhaden 2001; De Szoeke et al. 2007). The strong lateral and vertical shears between these different flow components can be unstable to barotropic and baroclinic instability (Philander 1976; Cox 1980). The dominant mode of instability manifests as a series of westward-traveling meridional oscillations in the equatorial fronts with observed wavelengths of 1000–1500 km and periods of 15–36 days (Legeckis 1977; Qiao and Weisberg 1995; Willett et al. 2006). These tropical instability waves (TIWs) can evolve into nonlinear anticyclonic tropical instability vortices (TIVs), which are only observed routinely to the north of the equator (Yu et al. 1995). The vortices have radii of 500 km centered around 4°–5°N, have velocities stronger than 1 m s^{-1}, and travel westward at phase speeds of order 0.3 m s^{-1} (Flament et al. 1996; Kennan and Flament 2000).

The strong vertical vorticity and associated horizontal circulation of an individual TIW or TIV brings colder upwelled water northward on its leading (western) side and warmer water southward on its trailing (eastern) side (Hansen and Paul 1984). This induces an equatorward eddy heat flux that may influence the heat budget of the equatorial region (Menkes et al. 2006), with implications for the ENSO cycle (Vialard et al. 2001; Yu and Liu 2003). TIWs and TIVs have been found to modulate vertical mixing in the high shear layer above the Equatorial Undercurrent (EUC) core (Lien et al. 2008; Moum et al. 2009; Inoue et al. 2012), which also has a strong influence on the equatorial heat budget (Moum et al. 2013).

Much of the past research on TIW and TIV dynamics has focused on stability analysis and energetics. Perturbations on a zonally and temporally independent

Corresponding author address: Ryan M. Holmes, Dept. of Environmental Earth System Science, Stanford University, 473 Via Ortega, Room 140, Stanford, CA 94305.
E-mail: rmholmes@stanford.edu

DOI: 10.1175/JPO-D-13-0157.1

background flow can extract energy from the background meridional shear (barotropic source), background meridional buoyancy gradient (baroclinic source), and background vertical shear (vertical shear production source; e.g., Proehl 1996). Early work concluded that the barotropic source constituted the main energy source for TIWs (Philander 1976, 1978; Hansen and Paul 1984; Qiao and Weisberg 1998). Baroclinic instability associated with the potential energy in the equatorial SST fronts was also thought to contribute (Cox 1980; Yu et al. 1995). More recent work has detailed the spatial distribution and relative importance of these energy source terms (Luther and Johnson 1990; Masina et al. 1999; Jochum et al. 2004; Johnson and Proehl 2004; Grodsky et al. 2005; Lyman et al. 2007).

In the case of TIVs, these instabilities result in the generation and/or accumulation of anticyclonic vorticity within the vortex core. TIVs exhibit high vorticity Rossby number (Ro $= \zeta/f$, where $\zeta = \partial v/\partial x - \partial u/\partial y$ is the vertical relative vorticity and f is the Coriolis parameter) dynamics with core water characterized by vorticity Rossby numbers reaching -1 (Kennan and Flament 2000), and thus, they have close to zero absolute vorticity and anomalously low potential vorticity (PV). The vortex dynamics leading to the generation and accumulation of their strong anticyclonic relative vorticity has so far received little attention. Foltz et al. (2004) used a layer-averaged PV to show that changes in the relative vorticity of water inside Atlantic TIVs were due to advection of relative and planetary vorticity. However, in not using the full Ertel PV, defined here as[1]

$$q = \boldsymbol{\omega} \cdot \nabla b = \underbrace{(f+\zeta)N^2}_{q_v} + \underbrace{\boldsymbol{\omega}_h \cdot \nabla_h b}_{q_h}, \tag{1}$$

they did not consider how horizontal density gradients and vertical shear, encompassed in the baroclinic component q_h, affect the PV and influence the vortex dynamics. The baroclinic component associated with the baroclinicity of the flow can be important relative to the vertical component q_v associated with the absolute vertical vorticity when the Richardson number (Ri $= N^2/|\partial \mathbf{u}_h/\partial z|^2$, where N^2 is the vertical buoyancy gradient or stratification and $\mathbf{u}_h$ is the horizontal velocity) of the flow is low. Indeed, Inoue et al. (2012) show that TIVs are associated with $O(1)$ Richardson numbers near the equator in the EUC shear layer, justifying an examination of the vortex dynamics of TIVs using the full version of the Ertel PV [Eq. (1)].

In the midlatitudes, the $O(1)$ Rossby and Richardson number regime defines submesoscale flows, with typical horizontal scales of 100 m to 10 km (Thomas et al. 2008). Thus, TIVs contain a range of flow features normally associated with midlatitude submesoscale physics, such as strong fronts, vertical velocities, ageostrophic flows, and frontogenesis (Marchesiello et al. 2011; Ubelmann and Fu 2011). In particular, they share features in common with submesoscale coherent vortices and intrathermocline eddies (ITEs), that is, lenticular coherent anticyclonic vortices that are found in the thermocline and that are characterized by water in their cores that has anomalously low PV (Dugan et al. 1982; McWilliams 1985; Kostianoy and Belkin 1989).

The core water in TIVs and fully formed ITEs is characterized by anomalously low values of PV due to near-zero absolute vorticity (Kennan and Flament 2000) and low stratification. Following Thomas (2008), we refer to this flavor of low PV as vertically low PV. A second flavor of low-PV water can occur in the presence of strong horizontal buoyancy gradients at fronts, where the PV can be baroclinically low because of the baroclinicity of the flow. For a 2D front in geostrophic and hydrostatic balance, the thermal wind relation is given by

$$\nabla_h b = f\frac{\partial \mathbf{u}_g}{\partial z} \times \hat{\mathbf{k}} = -f\boldsymbol{\omega}_h. \tag{2}$$

The baroclinic PV component associated with this flow is

$$q_{\mathrm{hg}} = \boldsymbol{\omega}_h \cdot \nabla_h b = -\frac{|\nabla_h b|^2}{f}, \tag{3}$$

which is negative definite in the Northern Hemisphere, and thus this component always decreases the PV. Baroclinically low PV water is common at submesoscale fronts in the midlatitudes where the inverse geostrophic Richardson number, obeying the relation $\mathrm{Ri}_g^{-1} = -q_{\mathrm{hg}}/fN^2$, is $O(1)$, and thus the baroclinic component q_h is strongly negative and compensates the vertical component q_v.

One proposed generation mechanism for ITEs involves the subduction of parcels of baroclinically low PV water generated at a submesoscale front (Thomas 2008). The subduction can be driven by the strong vertical velocities associated with frontogenesis (Spall 1995). As these subducting parcels of water with $q \approx 0$ follow sloped isopycnals into the thermocline, their horizontal buoyancy gradient decreases and q_h moves toward zero; conservation of total PV implies that q_v must also move

[1] In Eq. (1), $b = -g\rho/\rho_0$ is the buoyancy, g is acceleration due to gravity, ρ is the potential density, and ρ_0 is a reference density. The equation $\boldsymbol{\omega} = f\hat{\mathbf{k}} + \nabla \times \mathbf{u}$ is the absolute vorticity, with vertical component $f + \zeta$ and horizontal component $\boldsymbol{\omega}_h$, and $\hat{\mathbf{k}}$ is the local vertical unit vector.

toward zero. The parcel of water undergoes baroclinically low to vertically low PV conversion. The horizontal vorticity of the baroclinic frontal flow acts as a source for the anticyclonic vorticity of the developed ITE through vortex tilting (Thomas 2008).

The low Richardson numbers associated with TIVs near the equator suggest that the baroclinic component of the PV may be substantial and, similar to ITEs and submesoscale flows, may play a role in the vortex dynamics of TIV core water formation. This is in contrast to mesoscale eddies in the midlatitudes with similar horizontal scales as TIVs (~500 km), where q_h is negligible in comparison to q_v. However, the large meridional scale of a TIV implies that it is influenced by the gradient in planetary vorticity, and thus TIVs share some characteristics with both submesoscale and mesoscale flows in the midlatitudes.

The research presented here addresses several outstanding questions relating to the dynamics of TIVs. First, the vortex dynamics leading to the formation of their strong anticyclonic vorticity has not been described in detail. The low-PV water forming the TIV core could be sourced through advection from the Southern Hemisphere and equatorial region (Foltz et al. 2004; Dutrieux et al. 2008). Low-PV water could also be created locally by nonconservative processes, such as friction associated with down-front winds (Thomas 2005), surface cooling, or isopycnal mixing. A second outstanding problem is that of the dominant force balance and the frontal dynamics associated with TIVs. The strong rotation of TIVs suggests that centrifugal and other advective effects may be important. For Atlantic TIVs, Foltz et al. (2004) found that centrifugal forces were up to 50% as large as geostrophic effects. Analysis of observations from a front on the leading edge of a Pacific TIV suggests that the frontal currents follow a pressure gradient–advection balance rather than a geostrophic balance (Johnson 1996). These departures from geostrophic balance could have implications for the detailed frontal dynamics of TIVs and thus for the formation of their core water.

To address these questions, we use a nested simulation of the equatorial Pacific described in section 2. In this section we also give a general overview of the circulation associated with TIVs, and look at the dominant momentum balance. In section 3, we examine the physics of TIVs from a new perspective using Lagrangian analysis of the PV and vortex dynamics, following the methods of Thomas (2008) and Ubelmann and Fu (2011). We also describe the entrance pathways and formation mechanisms of TIV core water. Finally, in section 4, we examine the frontogenesis associated with TIVs, with implications for their vortex dynamics. The main results are discussed and summarized in sections 5 and 6.

2. Model and general flow description

a. Model setup

To examine the dynamics of TIVs, a set of 3D nested simulations of the equatorial Pacific at progressively higher resolutions was performed using the Regional Ocean Modeling System (ROMS; Shchepetkin and McWilliams 2005). A Pacific basin–wide simulation over the region −240° to −70°E, 30°S to 30°N with 0.25° horizontal resolution, 20 vertical levels, and a time step of 10 min was performed and spun up over a 10-yr period. Daily climatological surface forcing, initial conditions, and boundary conditions were taken from the Common Ocean Reference Experiment Normal Year Forcing field (Large and Yeager 2004). At the meridional boundaries, temperature and salinity were nudged to climatological values, while zonal and meridional velocities were nudged to zero. In addition, monthly climatological nudging was used in order to maintain the tropical thermocline. The K-profile parameterization (KPP) vertical mixing scheme was used to parameterize subgrid-scale vertical mixing processes (Large et al. 1994).

In the last year of the basinwide simulation, a 0.05° midresolution simulation was nested within the region −145° to −120°E, 5°S to 10°N. Finally, a 0.025° (~3 km) high-resolution simulation was nested inside the midresolution simulation with 40 vertical levels (~9-m resolution in the top 100 m) and a time step of 1 min. Both inner nests have horizontal resolutions (6 and 3 km, respectively) below the 10 km reported by Marchesiello et al. (2011) as required for numerical convergence as measured by an invariance of the kinetic energy spectrum with resolution. On the inner nests, a combination of nudging and radiation boundary conditions is used, with the exception of a clamped condition on the eastern boundary tracers. Horizontal diffusion of momentum is achieved through a biharmonic viscosity with the coefficients 1×10^9 (high resolution), 1×10^{10} (midresolution), and $1 \times 10^{11}\,\mathrm{m^4\,s^{-1}}$ (basin wide), and the horizontal diffusion of salinity and temperature is achieved through a harmonic diffusion with the coefficient $100\,\mathrm{m^2\,s^{-1}}$. ROMS has been successfully used for process studies of TIWs under a similar configuration (Marchesiello et al. 2011).

b. Properties of model TIVs

The simulations produce TIWs that commence around May and die off the following January. TIWs are visible as cusps in the SST fields at the north and south

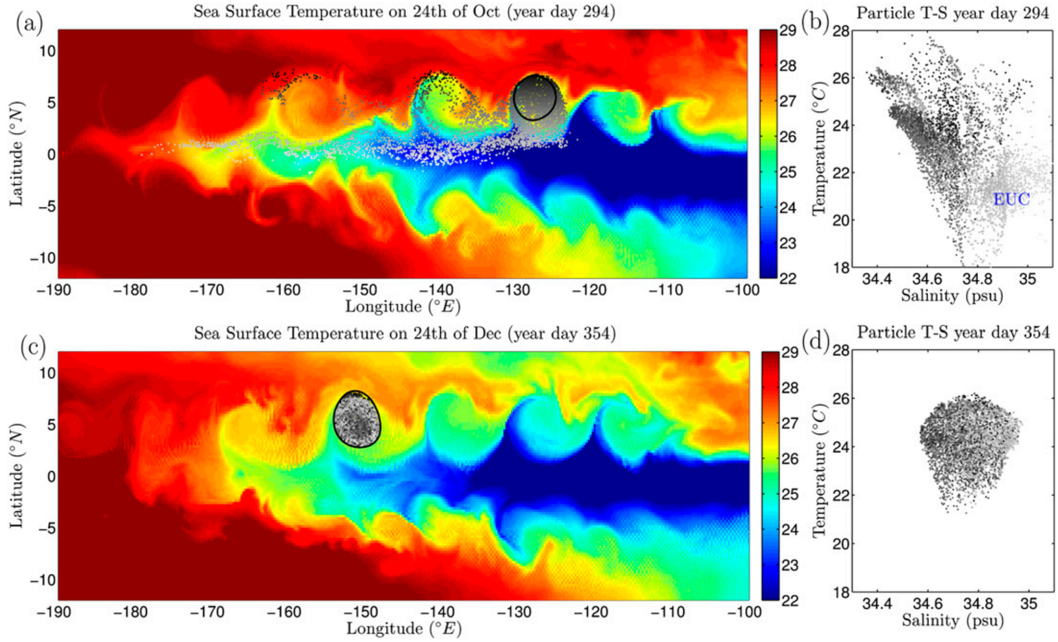

FIG. 1. (a),(c) Model SST and (b),(d) temperature–salinity diagram for particles inside a TIV on (top) 24 Oct and (bottom) 24 Dec. The particles are shaded according to their latitude on 24 Oct and the TIV streamfunction contour is plotted with the black line. Water from the EUC and the NECC combine and experience significant Lagrangian changes in temperature and salinity [cf. (b) and (d)] to form TIV core water. The EUC water mass, corresponding to the cold and salty water coming from more southern latitudes, is indicated in (b).

equatorial fronts (Fig. 1) and are accompanied by anticyclonic vortices (TIVs) in the Northern Hemisphere. The properties of the model TIVs and their fronts compare favorably with the observations of Flament et al. (1996), Kennan and Flament (2000), and Johnson (1996), suggesting that the numerical solutions and the observations are dynamically similar, as discussed below.

For the purposes of tracking and locating TIVs and determining whether Lagrangian particles are inside or outside TIVs, we define a control volume that covers the extent of a TIV using a surface streamfunction[2] Ψ condition, as in Dutrieux et al. (2008). The center of each vortex is identified as being a local minimum in the streamfunction. We then define the horizontal extent of the vortex as that Ψ contour enclosing an instantaneous surface closed circulation around the vortex of $\sim 0.23 \times 10^6\,\mathrm{m^2\,s^{-1}}$. This streamfunction contour (shown in Figs. 1a,c and 2a,d) is sufficient for the purposes of tracking TIVs. We define the vertical extent of the TIV using the 1022.8 and 1024.3 $\mathrm{kg\,m^{-3}}$ isopycnal surfaces (Figs. 2b,e).

The vortex is characterized by anticyclonic vertical vorticity of a magnitude similar to the Coriolis parameter. This is reflected in the vorticity Rossby number of order -1 (Fig. 2c) and near-zero q_v in the vortex core (Fig. 3a). TIVs with vorticities of this magnitude have been observed (i.e., Fig. 15 of Kennan and Flament 2000). The vortex depresses the thermocline and is associated with anomalously low stratification along isopycnal layers that are midthermocline to the north, east, and west (Figs. 2b, 3c), highlighting its similarity to an ITE (Thomas 2008). The baroclinic component of the PVq_h (Figs. 3b,d) tends to be negative, with a magnitude comparable to that of q_v (cf. Figs. 3a with 3b and 3c with 3d) in regions of strong horizontal buoyancy gradients, which here are found on the western leading edge of the vortex and in the EUC shear layer to the south (Fig. 4). On the western edge of the vortex, cold water is advected northward from the upwelling region through the TIW cold cusp region (the cusp of cold water with SST between 20° and 25°C in Fig. 2a at the leading edge of the vortex). The flow in this region is confluent, with the cold water moving northward and westward faster than the warmer water to its north, driving strong frontogenesis. This confluent flow intensifies the north equatorial front here, producing a strong SST front at the leading edge of

[2] The streamfunction Ψ was calculated by solving the Poisson equation $\nabla^2\Psi = -\zeta_s$, where $\zeta_s = \partial v_s/\partial y - \partial u_s/\partial y$ with (u_s, v_s) the surface velocities in the (x, y) directions, at each time using Dirichlet boundary conditions derived by integrating the conditions $\partial\Psi/\partial y = u_s$, $\partial\Psi/\partial x = -v_s$ around the perimeter of the domain.

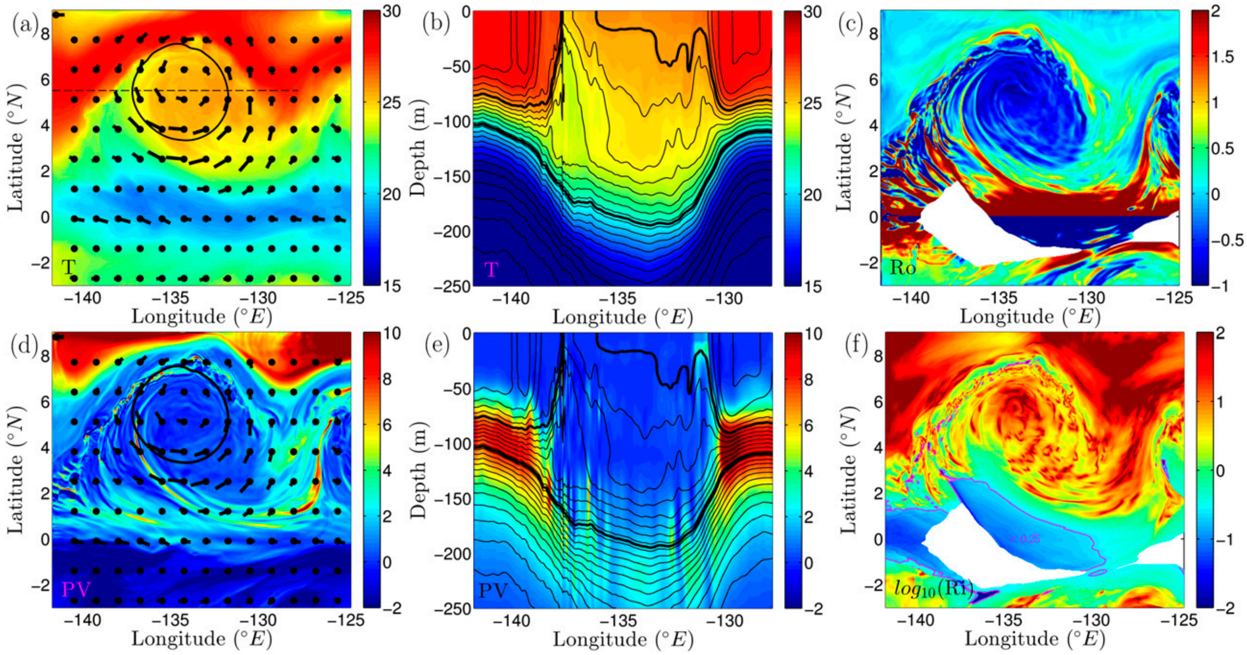

FIG. 2. Horizontal slices of (a) temperature (°C) and (d) PV ($\times 10^{-9}\,s^{-3}$) through a TIV at 50-m depth in the high-resolution simulation. Horizontal velocity vectors are shown with the round marker indicating the tail of the vector. For scaling, a 1 m s^{-1} velocity vector is shown in the top left-hand corner of (a) and (d). The streamfunction contour enclosing a transport of $\sim$0.23 Sv m^{-1} (1 Sv $\equiv 10^6\,m^3\,s^{-1}$) is also shown in (a) and (d). Vertical slices of (b) temperature and (e) PV at 5.5°N. The thin black lines represent isopycnals with a spacing of 0.2 k gm^{-3}, and the thick lines are the 1022.8 and 1024.3 kg m^{-3} isopycnals bounding the TIV control volume. (c) The vorticity Rossby number (Ro = ζ/f) and (f) the log of the Richardson number (Ri = $N^2/|\partial u/\partial z|^2$) averaged over the isopycnal layer bounded by the thick isopycnals. All plots are on 11 Oct (yearday 281.2083).

the cold cusp [leading-edge front (LEF) in Fig. 4], where the surface temperature changes by up to 3°C over $\sim$10 km and rapid subduction (at rates of $\sim$0.5 cm s^{-1}) of the cold equatorial water occurs [consistent with the observations of Johnson (1996), who observed subduction rates of up to 0.9 cm s^{-1}]. High gradients in PV and vorticity are visible across the frontal jet (Figs. 2c,d).

On the east side of the cold cusp, the north equatorial front bends back toward the equator in the southwest corner of the TIV. Here there is a less intense front on the trailing edge of the TIW cold cusp [trailing-edge front (TEF) in Fig. 4]. Filaments of low PV are entrained into the vortex through this region (Fig. 2d), suggesting that this region may provide a source for the water that forms the TIV core. This region is characterized by high vertical shear associated with the EUC shear layer, where the Richardson number is frequently below the critical value for vertical shear instability of ¼ (Fig. 2f). The shear and Richardson number above the EUC are modulated by the presence of the TIV, in agreement with the observations of Lien et al. (2008). The westward surface flow induced by the southern part of the vortex over the EUC core increases the vertical shear, and thus a decrease in the Richardson number occurs at longitudes coincident with the span of the vortex (Fig. 2f). The vertical shear has an associated southward-pointing horizontal vorticity, which, when coupled with the buoyancy gradient associated with the north equatorial front, results in a large negative q_h (Fig. 3b), of the same order of magnitude as q_v. The importance of this store of baroclinically low PV is discussed further in section 3.

c. Force balance

The question of whether geostrophic balance and thermal wind balance are dynamical constraints at the equator is important for the frontogenesis mechanism discussed in section 4. Here we calculate the percentage error in the geostrophic and cyclogeostrophic balances using the model output diagnostics. The geostrophic (GB) and cyclogeostrophic (CGB) force balances are expressed as

$$\text{GB: } -\frac{1}{\rho_0}\nabla_h P - f\hat{\mathbf{k}}\times\mathbf{u} = 0 \quad \text{and} \tag{4}$$

$$\text{CGB: } -\frac{1}{\rho_0}\nabla_h P - f\hat{\mathbf{k}}\times\mathbf{u} - \mathrm{Proj}_{\hat{\mathbf{k}}\times\mathbf{u}}(\mathbf{u}\cdot\nabla\mathbf{u}) = 0, \tag{5}$$

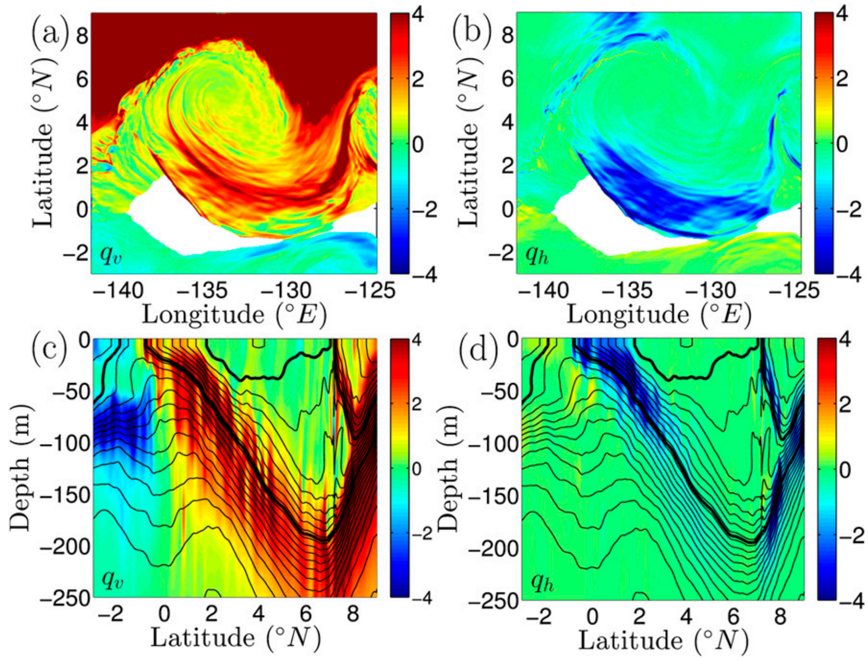

FIG. 3. The (a),(c) vertical and (b),(d) baroclinic components of the PV ($\times 10^{-9}\,\mathrm{s}^{-3}$) in the high-resolution simulation. The thin black lines represent isopycnals with a spacing of $0.2\,\mathrm{kg\,m}^{-3}$, and (top) the horizontal slices are averaged over the isopycnal layer bounded by the thick 1022.8 and $1024.3\,\mathrm{kg\,m}^{-3}$ isopycnals. (bottom) The vertical slices are at −135°E. All plots are on 11 Oct (yearday 281.2083).

where the first term is the pressure gradient force, the second term is the Coriolis force, and the third term in Eq. (5) is the centrifugal force, being the portion of horizontal momentum advection perpendicular to the horizontal velocity. The projection operator is defined as $\mathrm{Proj}_{\mathbf{b}}(\mathbf{a}) = (\mathbf{a}\cdot\hat{\mathbf{b}})\hat{\mathbf{b}}$, where $\hat{\mathbf{b}} = \mathbf{b}/|\mathbf{b}|$. The percentage error in the departure from these balances is expressed [following a method similar to Capet et al. (2008)] as

$$\gamma_{\mathrm{GB}} = \frac{\left|\dfrac{1}{\rho_0}\nabla_h P + f\hat{\mathbf{k}}\times\mathbf{u}\right|}{\left|\dfrac{1}{\rho_0}\nabla_h P\right| + |f\hat{\mathbf{k}}\times\mathbf{u}|}\times 100 \quad \text{and} \tag{6}$$

$$\gamma_{\mathrm{CGB}} = \frac{\left|\dfrac{1}{\rho_0}\nabla_h P + f\hat{\mathbf{k}}\times\mathbf{u} + \mathrm{Proj}_{\hat{\mathbf{k}}\times\mathbf{u}}(\mathbf{u}\cdot\nabla\mathbf{u})\right|}{\left|\dfrac{1}{\rho_0}\nabla_h P\right| + |f\hat{\mathbf{k}}\times\mathbf{u}| + |\mathrm{Proj}_{\hat{\mathbf{k}}\times\mathbf{u}}(\mathbf{u}\cdot\nabla\mathbf{u})|}\times 100, \tag{7}$$

so a 0% error indicates a perfectly balanced flow.

Geostrophic balance appears to hold throughout much of the domain at 33-m depth, with percentage error mostly less than 30% for latitudes greater than ±2° (Fig. 5a). A notable exception to this is within the vortex, where larger errors are seen, in particular in the northern part of the vortex. The curvature throughout the vortex is high, and thus the centrifugal term becomes important. The vortex is closely in cyclogeostrophic balance (Fig. 5b), with only the zero-velocity center of the vortex appearing to be out of balance (an artifact of

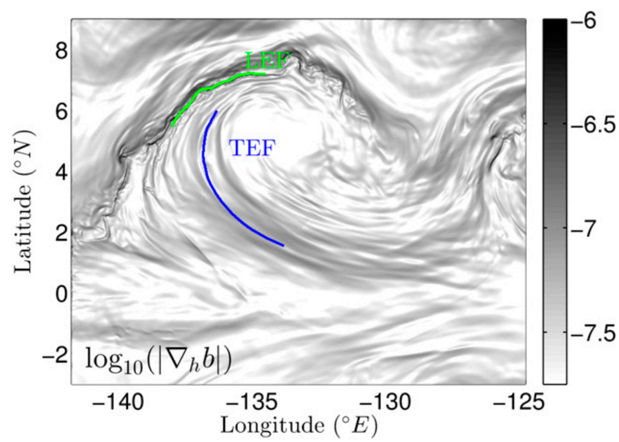

FIG. 4. The log of the magnitude of the horizontal buoyancy gradient [$\nabla_h b$ (s^{-2})] at 50-m depth in the high-resolution simulation on 11 Oct (yearday 281.2083). The location of the LEF (green line), defined by the position of a high-PV filament at 33-m depth, and the TEF (blue line), defined by the outcrop location of the $1022.9\,\mathrm{kg\,m}^{-3}$ isopycnal, are shown.

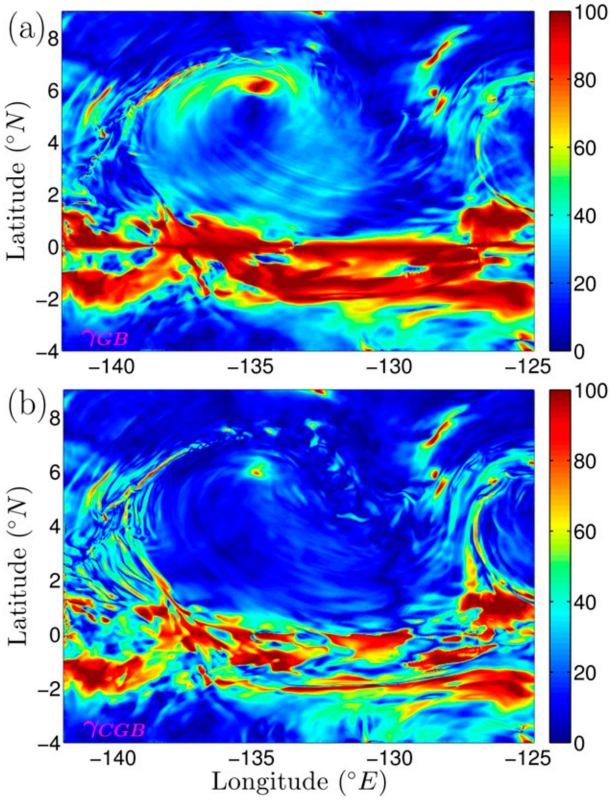

FIG. 5. Plots of the percentage error in the (a) geostrophic and (b) cyclogeostrophic force balances at 33 m depth from Eqs. (6) and (7). The flow is closely in geostrophic balance in most regions, even within a few degrees of the equator. The regions of the flow with high curvature inside the vortex and the region where the vortex flow penetrates over the equator are characterized by currents that are more accurately described by the cyclogeostrophic balance. The fields are evaluated on 12 Oct (yearday 282.7917).

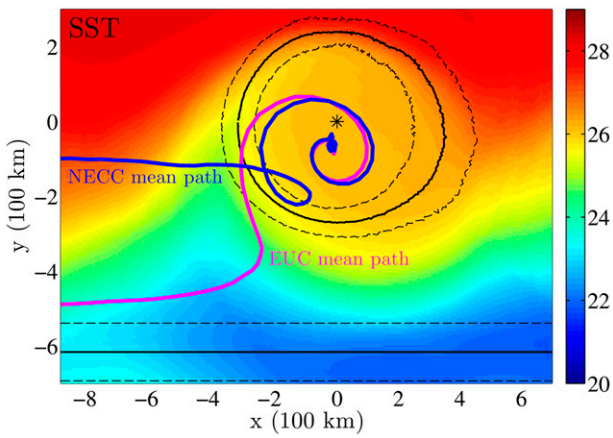

FIG. 6. Composite average SST field (°C) calculated by averaging the SST fields for each vortex at each day in the midresolution simulation around their center point, identified by the minimum in the surface streamfunction. This center point is shown by the black star, with the solid and dashed lines indicating the mean and ±2 standard deviation radial position of the TIV control volume streamfunction contour. The mean and ±2 standard deviation positions of the equator are also shown. The tracks shown are the center of mass tracks for particles coming from the EUC and particles coming from the NECC. We classified particles as NECC particles vs EUC particles if they passed above the latitude of 5°N between 2 months and 15 days before entering the TIV (i.e., they passed north of the center of the next TIV to the west).

the near-zero local pressure gradient force and velocity). In particular, where the flow of the vortex penetrates close to the equator, the cyclogeostrophic balance holds while the geostrophic balance breaks down (cf. Figs. 5a,b). This indicates that the strong curvature and rotation of the vortex act to constrain the flow and provide a diagnostic force balance that would not otherwise exist at the equator. The vortex is thus responsible for the balance asymmetry around the equator, where the region between 0° and 2°S appears out of cyclogeostrophic balance while the region between 0° and 2°N is more closely in cyclogeostrophic balance.

3. Lagrangian analysis of TIV core water formation

To investigate the source of the low-PV core water, we performed Lagrangian particle track calculations. The TIV cores in the basinwide and midresolution simulations were seeded throughout the season with Lagrangian particles having 5-m vertical spacing and grid-resolution horizontal spacing. The particles were then advected offline backward in time for several hundred days in the basinwide simulation and 2 months in the midresolution simulation to determine their source regions. The output time frequency used for the backward integration was once per day.

Many of the particles in an example trajectory calculation in the basinwide simulation remain in the same TIV for 2 months as it translates westward (cf. particle positions in Fig. 1c on 24 December and in Fig. 1a 2 months earlier), indicating that TIVs do transport a considerable amount of water zonally. At the same time, many particles enter the TIV from the west, mostly through the EUC and some through a more northern pathway encompassing the North Equatorial Counter Current (NECC) to the north and TIVs to the west [consistent with the findings of Dutrieux et al. (2008) for TIVs in the Atlantic]. Average or center of mass tracks can be calculated using the midresolution particles for these two entrance pathways (Fig. 6), confirming that most particles enter from the west through the southwest corner of the TIV.

Considerable changes in temperature and salinity occur along the Lagrangian fluid tracks entering the TIVs, with a predominant tendency for homogenization

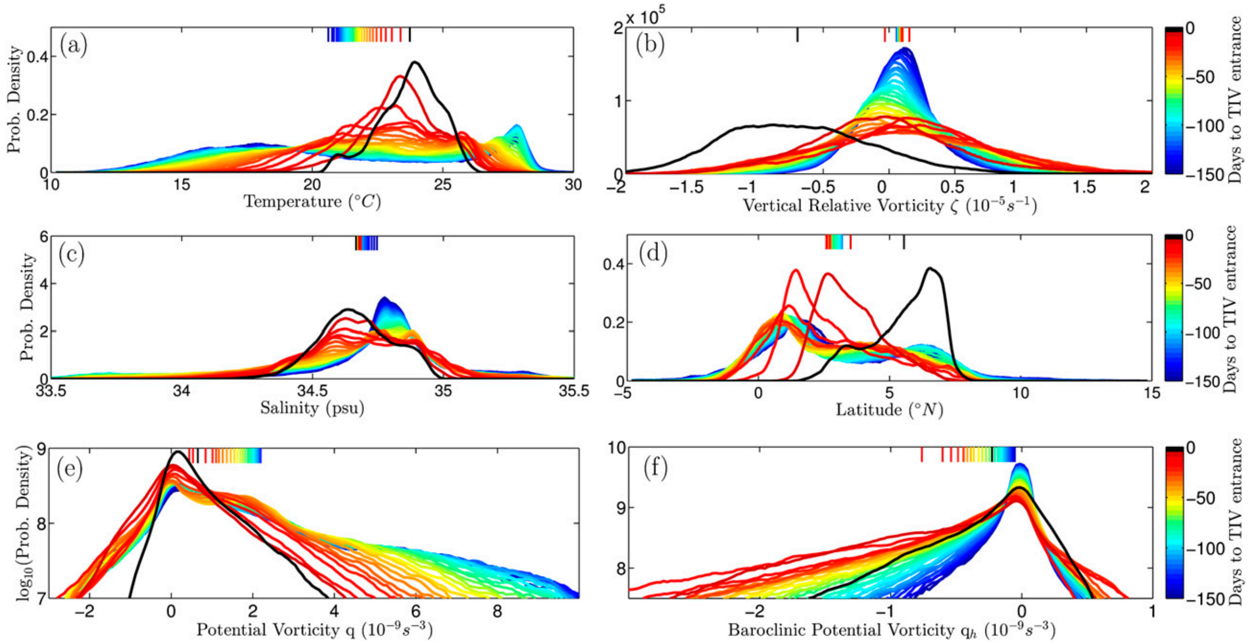

FIG. 7. Particle PDFs for (a) temperature, (b) vertical relative vorticity, (c) salinity, (d) latitude, (e) PV, and (f) baroclinic PV in the basinwide simulation on a shifted time axis relative to the time at which each particle enters the TIV in which it was seeded. The black curve in each plot represents the PDF of a tracer over the particles at the time at which each particle enters the TIV (day 0), which corresponds to a different calendar day for each particle. The colored curves represent the distribution over the particles of each tracer at 5-day intervals up to 150 days (dark blue curve) before the TIV entrance. Over 480 000 particles were used to calculate each PDF, and the number of particles in each PDF is the same. The PDFs are compilations over particles that enter the TIVs in the months September–December over the longitude range (−160° to −110°E). The distribution means are represented as straight ticks at the top of the plots.

(cf. Figs. 1b,d). This indicates that nonconservative processes may be important in forming the properties of the core water of TIVs. To investigate these changes, the evolution in time of probability distribution functions (PDFs) for various tracers can be calculated over the Lagrangian particles (Fig. 7). For each particle, a shifted time axis is defined with day 0 as that time when the particle first enters the control volume of the TIV in which it was seeded. The differences between the tracer PDFs at day 0 (black curve in Figs. 7a,c,e) and for earlier times (at 5-day intervals up to 150 days before TIV entrance; colored curves in Figs. 7a,c,e) confirm that considerable Lagrangian changes occur.

The PDFs for temperature and latitude (Figs. 7a,d) are consistent with the idea that TIV core water is sourced from the EUC and NECC. The temperature PDF describes mixing between water masses of two different temperature ranges, one with a narrow temperature distribution around 28°C (consistent with NECC water) and the other with a broad temperature distribution between 12° and 22°C (consistent with EUC water). The latitude PDFs at early times (blue curves in Fig. 7d) show two distinct peaks around 1° and 6.5°N. The 1°N EUC peak is large, indicating that this is the dominant water source. In particular, this PDF shows that very little of the TIV core water is sourced recently from the Southern Hemisphere, in contrast to the results of Foltz et al. (2004), who found that TIVs in the western Atlantic were sourced partially from Southern Hemisphere water. The peak of the latitude PDF around 2.5°N at −5 days (darkest red curve in Fig. 7d) and its subsequent movement north indicates that the majority of particles enter TIVs from the south beginning in their southwest corner. This is consistent with the center of mass tracks (Fig. 6), where the dominant entrance pathway for TIV water is from the southwest. Averaged over the particles, the dominant sign of the radial buoyancy gradient (measured relative to TIV centers) is negative at the entrance time (not shown), indicating that most particles enter through the weaker frontal region (the TEF in Fig. 4) on the east side of the cold cusp. The evolution of the PDF of particle depths (not shown) shows that the particles are closest to the surface in this TEF region and subduct around the time that they enter the TIV control volume.

The salinity PDF (Fig. 7c) describes a general freshening as the particles begin in the saltier western Pacific and move toward the fresher eastern Pacific before entering the TIVs. The distribution means show a gradual increase in temperature and a gradual decrease in salinity

(Figs. 7a,c). This implies that the particles' density decreases and suggests that external surface forcing and/or mixing is acting. A composite average of the surface buoyancy flux (calculated as in Fig. 6; not shown) suggests that heating of EUC water close to the surface in the TIW cold cusp may be responsible for the increase in mean temperature. Mixing with water masses not tagged with particles could also explain both the salinity and temperature changes. The changes in distribution shapes are most rapid at times around when the particles enter the TIVs (Fig. 7). This indicates that mixing between the water masses that were tagged with the particles is occurring leading up to the TIV entrance time, emphasizing the fact that TIVs homogenize tracers. These nonconservative effects are the subject of current research and will be presented in a subsequent paper.

The vertical relative vorticity distribution is skewed slightly toward cyclonic values at early times (Fig. 7b), consistent with the northern portion of the EUC. However, in the last 5 days before particles enter the TIVs, they acquire considerable anticyclonic vorticity. The development of this strong anticyclonic vorticity will be examined in the next section.

The distribution for the PV (Fig. 7e, plotted on a log scale) describes a systematic decrease as PV is lowered (the high-PV tail disappears) to the values present in the TIV core. The mean has a steady decrease, indicating that diabatic and/or frictional processes may be occurring. Similar to the other tracers, these changes appear to be most rapid just before the particles enter the TIVs, when the particles are in the vicinity of the cold cusp and close to the frontal regions in this area. This suggests that frontal processes may play a role in controlling the change of properties along Lagrangian tracks and may influence the key process of PV lowering.

The importance of frontal processes and stores of baroclinically low PV are quantified in the PDF of q_h (Fig. 7f, plotted on a log scale). This PDF is skewed toward negative values, suggesting that the horizontal vorticity is most often pointing in the opposite direction to the horizontal buoyancy gradient. This is expected given that the geostrophic and thermal wind balance [giving a negative-definite q_h as in Eq. (3)] holds in much of the domain (Fig. 5a). However, positive values do make a considerable contribution, indicating that ageostrophic shears are present. The q_h distribution mean is initially of small magnitude (blue curves in Fig. 7f) and becomes more strongly negative as the frontal regions around the TIVs and the north equatorial front are approached. Finally, between day -5 and day 0 (darkest red and black curves in Fig. 7f), a rapid decrease in magnitude of q_h occurs, where much of the negative tail in the distribution disappears. This, along with the rapid development of anticyclonic vertical vorticity (Fig. 7b), may indicate that the baroclinically low PV is being converted to vortically low PV as the particles enter the TIVs. We quantify this in the next section using diagnostics of the PV and vertical vorticity.

Potential vorticity and vorticity dynamics of TIVs

First, we consider an example set of 56 particles entering a TIV that were advected online in the high-resolution simulation (Fig. 8). These particles follow a path similar to the EUC center of mass entrance pathway (Fig. 6), moving into the vortex southwest corner while descending in the vertical (Fig. 8c). We perform a Lagrangian analysis of various properties along the particle tracks (Fig. 9). Prior to interpolation onto the particle tracks, fields were spatially filtered with a 14-km/five-grid-point horizontal filter followed by a three-grid-point vertical filter. An ensemble average was then performed over the 56 particles in order to average over the high spatial variability in the underlying fields (this spatial variability is represented by the error bars in Fig. 9).

A Lagrangian analysis of the various components of the Ertel PV [Eq. (1)] shows that the 56 particles have low PV throughout their path (Fig. 9a). However, at the initial time (yearday 283.4), their low PV is attributable to near cancellation between the baroclinic (q_h in Fig. 9a) and vertical (q_v in Fig. 9a) components. At this time, the particles are at the northern end of the EUC shear layer and their baroclinically low PV comes from the strong vertical shear in this region (e.g., Fig. 2f). This baroclinically low PV is surface intensified (Fig. 8c), and over the time period from yearday 283.5 to 284.5, the particles subduct (Fig. 8c) and move to the northern side of the vortex (Fig. 8a), out of the baroclinically low PV region. At late times (after yearday 284.5), the PV is still low, as required by the near conservation of PV, but now both the vertical and baroclinic components are near zero (Fig. 9a). The terms fN^2 and ζN^2 nearly cancel, and the PV is vortically low because of a near-zero absolute vertical vorticity. The particles have obtained strong anticyclonic vorticity with values approaching $-f$, typical of the flow in the TIV core.

To understand this creation of negative vertical relative vorticity ζ, we examine the Lagrangian evolution equation for the vertical relative vorticity:

$$\frac{D\zeta}{Dt} = -v\frac{df}{dy} + (f+\zeta)\frac{\partial w}{\partial z} + \frac{\partial u}{\partial z}\frac{\partial w}{\partial y} - \frac{\partial v}{\partial z}\frac{\partial w}{\partial x} + (\nabla \times \mathbf{F})\cdot\hat{\mathbf{k}}, \tag{8}$$

where $\mathbf{F}$ denotes the frictional force in the momentum equations, parameterized using the KPP mixing scheme and a horizontal biharmonic viscosity in ROMS. We have

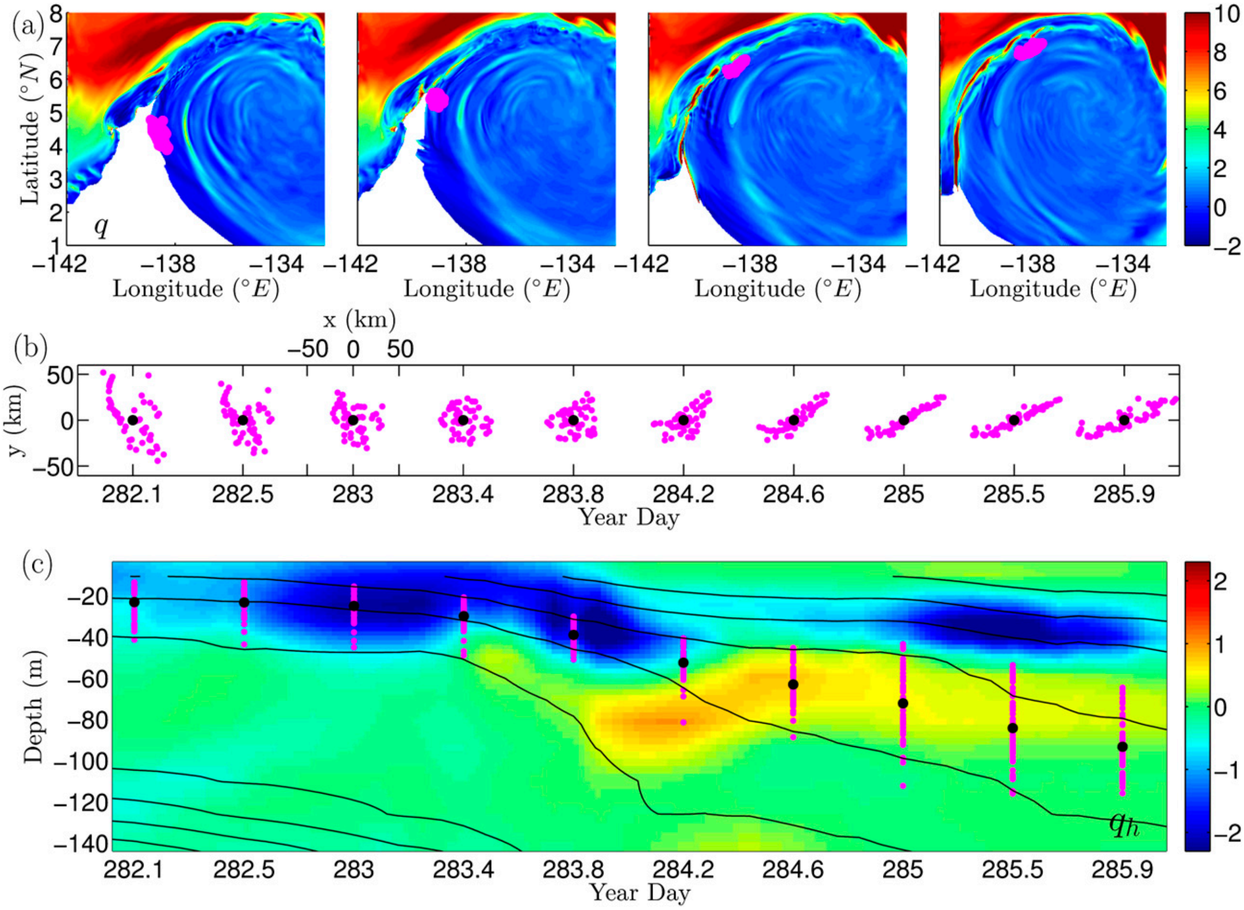

FIG. 8. (a) Positions of 56 particles at yeardays 282, 283⅓, 284⅔, and 286 lying close to the 1023.45 kg m^{-3} isopycnal surface in the high-resolution simulation. The field plotted on the isopycnal is PV ($\times 10^{-9}$ s^{-3}), with the isopycnal outcrop on the edge of the blank regions. (b) Horizontal distribution of particle positions relative to the particles' center of mass as a function of time. (c) Depth–time slice of q_h ($\times 10^{-9}$ s^{-3}) along the particle center of mass track. The thin black lines represent isopycnals with a spacing of 0.2 kg m^{-3}. The vertical positions of the particles are shown at times corresponding to those in (b).

not included the negligible solenoidal term (Ubelmann and Fu 2011). Performing an ensemble average over the particles (denoted by angle brackets) and a Lagrangian time integral along the particle tracks (denoted $\int_{\mathcal{L}} dt$) allows the total change in vorticity $\delta\zeta = \int_{\mathcal{L}} (D\zeta/Dt)\, dt$ to be attributed to terms on the right-hand side of Eq. (8):

$$\begin{aligned} \mathrm{BETA} &= \int_{\mathcal{L}} \left\langle -v\frac{df}{dy} \right\rangle dt, \\ \mathrm{STR} &= \int_{\mathcal{L}} \left\langle (f+\zeta)\frac{\partial w}{\partial z} \right\rangle dt, \\ \mathrm{TILT} &= \int_{\mathcal{L}} \left\langle \frac{\partial u}{\partial z}\frac{\partial w}{\partial y} - \frac{\partial v}{\partial z}\frac{\partial w}{\partial x} \right\rangle dt, \\ \mathrm{FRIC} &= \int_{\mathcal{L}} \langle (\nabla \times \mathbf{F}) \cdot \hat{\mathbf{k}} \rangle\, dt. \end{aligned} \tag{9}$$

Thus, changes in the vertical relative vorticity can occur through meridional advection of planetary vorticity (BETA), stretching of vertical vorticity (STR), tilting of horizontal vorticity into vertical vorticity (TILT) and frictional torques (FRIC). In the analysis shown below, we calculate the tilting term as a residual of the other terms,

$$\mathrm{TILT} = \delta\zeta - \mathrm{STR} - \mathrm{BETA} - \mathrm{FRIC}, \tag{10}$$

to minimize the error due to finite difference truncation, which is worse for the tilting term than the other terms as it contains the horizontal derivative of the vertical velocity. However, calculation of the direct tilting term from Eq. (9) (not shown) gives a qualitatively similar result and does not change the conclusions below.

A Lagrangian analysis of these terms along the particle tracks (Fig. 9b) shows that the decrease in relative vorticity $\delta\zeta$ comes primarily from vortex tilting (TILT in Fig. 9b), where the horizontal vorticity associated with the EUC shear layer (and associated with q_h in Fig. 9a) is

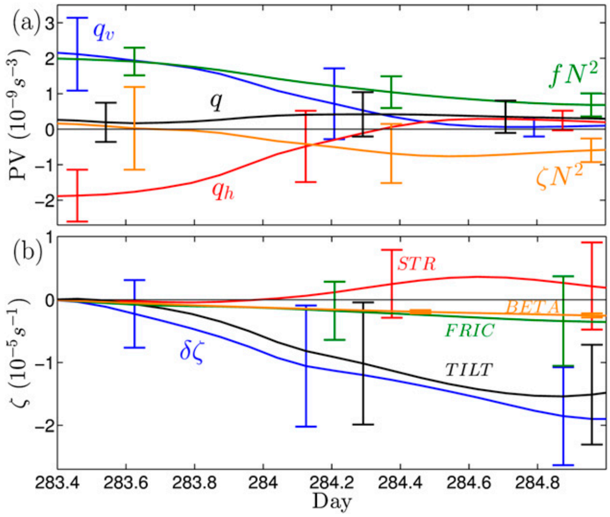

FIG. 9. Ensemble-averaged Lagrangian time series of the different terms (a) in the Ertel PV [Eq. (1)] and (b) in the time-integrated vertical relative vorticity equation [Eq. (8)] made following the 56 particles shown in Fig. 8. In (a), q is the total PV split into vertical q_v and baroclinic q_h parts. The vertical term is further split into planetary fN^2 and relative ζN^2 vorticity components. In (b), $\delta\zeta$ is the change in relative vorticity, TILT represents changes in ζ driven by vortex tilting, STR by vortex stretching/squashing, FRIC by frictional torques, and BETA by advection of planetary vorticity [see Eq. (9)]. The error bars represent the ± 1 standard deviation spread over the particle ensemble caused by spatial variability in the underlying fields over the span of the floats.

tilted downward to form anticyclonic vertical vorticity. This term dominates the change in ζ (Fig. 9) as the particles subduct and leave the surface frontal region between yeardays 283.5 and 285 (Fig. 8c). There are also contributions from frictional effects (FRIC in Fig. 9b) and from advection of planetary vorticity (BETA in Fig. 9b), although they are not sufficient to explain the development of strong anticyclonic vorticity without vortex tilting. The vortex stretching term is positive (STR in Fig. 9b) but is dominated by the other terms. This positive stretching is associated with a reduction in stratification of the source water to levels appropriate for the TIV core.

The process of baroclinically low to vertically low PV conversion demonstrated above can provide a source for the anticyclonic rotation of the TIV by purely conservative processes. This source is conservative because the increase in q_h is compensated by a reduction in ζ such that the total PV [Eq. (1)] remains constant (Fig. 9a). Other possible conservative sources for ζ could be changes in stratification N^2 through vortex stretching and changes in f along the fluid tracks through advection of planetary vorticity. However, nonconservative changes in the total PV q could also give rise to changes in vorticity as well.

To quantify the relative importance of these different sources of anticyclonic vorticity to TIVs, we calculated the amount of ζ that would be acquired given the observed change in q_h, q, f, and N^2 on particles run offline in the midresolution simulation. The following calculation includes particles that enter three TIVs in the midresolution simulation from any source, including both the EUC and NECC, and thus is a global calculation over all TIV core water sources in contrast to the specific calculation in Figs. 8 and 9 used to demonstrate the PV conversion mechanism associated with q_h.

Rearranging the equation for the PV [Eq. (1)] and normalizing by a mean $\overline{N^2} = 1.6 \times 10^{-4}\,\mathrm{s}^{-2}$ and mean $\overline{f} = 1.27 \times 10^{-5}\,\mathrm{s}^{-1}$ appropriate for the vortex center at 5°N gives

$$\frac{\Delta\zeta}{\overline{f}} = \underbrace{\frac{\Delta q}{\overline{f}\overline{N^2}}}_{\delta_q} - \underbrace{\frac{\Delta f}{\overline{f}}}_{\delta_{-f}} - \underbrace{\frac{\Delta q_h}{\overline{f}\overline{N^2}}}_{\delta_{-q_h}} - \underbrace{\frac{(\overline{f} + \overline{\zeta})\Delta N^2}{\overline{f}\overline{N^2}}}_{\delta_{N^2}} . \quad (11)$$

We choose Δ to represent a net change for each particle from 4 days before it enters the TIV control volume to 1 day afterward, as this is when most of the change in ζ occurs. The mean $\overline{\zeta}$ was defined as the average ζ over this same period for each particle. For each particle that experiences a decrease in ζ of at least $-0.5 \times 10^{-5}\,\mathrm{s}^{-1}$ over this period, we calculate δ_q, δ_{-f}, δ_{-q_h}, and δ_{N^2}, where we use the same spatial filtering as for Fig. 9.

For ~100 000 particles in the midresolution simulation that satisfy the ζ decrease condition, a PDF was calculated of each term in Eq. (11) (Fig. 10). The major contributor to the decrease in ζ for particles entering the TIVs is the advection of planetary vorticity δ_{-f}. This distribution has a mean of -0.58, suggesting that northward advection of planetary vorticity results in reduction of ζ of order half a vorticity Rossby number. The contribution of nonconservative processes (δ_q in Fig. 10) has a PDF that is nearly symmetrically distributed around zero, apart from a slight negative tail associated with a preference for PV reduction. The contribution from changes in stratification (δ_{N^2} in Fig. 10) is minor and generally acts to increase ζ through vortex stretching as the stratification reduces entering the vortices. The baroclinic term (δ_{-q_h} in Fig. 10) provides a significant contribution to this global calculation (mean -0.35) that is systematically negative. Thus, the horizontal vorticity of TIV source water cannot be neglected as it generates considerable anticyclonic vorticity for TIVs.

The Lagrangian analysis above focuses on changes in relative vorticity and by its nature does not take into account advection of the initial relative vorticity distribution. The evolution of vorticity along the particle

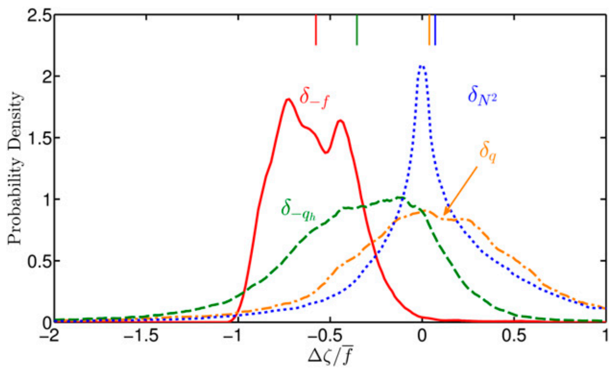

FIG. 10. PDFs of the contribution to reductions in vertical vorticity $\Delta\zeta$ driven by the different terms in the PV given in Eq. (11). This is a global calculation over all TIV core water sources that considers ~100 000 particles that enter three TIVs in the midresolution simulation. The vorticity is normalized by $\overline{f} = 1.27 \times 10^{-5}\,\mathrm{s}^{-1}$, a value of the planetary vorticity representative of the vortex center at 5°N. The change in vorticity is calculated over a 5-day period starting 4 days before the particles enter the TIV and ending 1 day after they enter, with only decreases in ζ of more than $-0.5 \times 10^{-5}\,\mathrm{s}^{-1}$ considered. The fields are filtered in space (five grid points in the horizontal, three points in the vertical, as in Fig. 9) before interpolation onto particle tracks. The variable δ_{-f} represents the change in ζ due to advection of planetary vorticity, δ_{N^2} represents the change due to changes in stratification (vortex squashing/stretching), δ_{-q_h} represents the change due to changes in the baroclinic PV (vortex tilting), and δ_q represents the change to nonconservative changes in PV [all from Eq. (11)].

paths (Fig. 7b) shows that the vorticity distribution of particles is initially skewed toward cyclonic values and changes considerably on entering the TIV. There is only minor overlap between the vorticity distributions at early times with the distribution as the particles enter the TIVs. The TIVs will go on to homogenize absolute vorticity within their cores (not shown in Fig. 7b), and thus the relative vorticity distribution has little memory of its initial distribution and advection of relative vorticity has a minor influence.

The process of baroclinically low to vertically low PV conversion generates some of the anticyclonic rotation of TIV core water. This process can be understood schematically by assuming for simplicity that the PV remains zero throughout the conversion process (Fig. 11). A water parcel in the EUC shear layer can have zero PV because of cancellation between the projection of the horizontal vorticity and that of the vertical vorticity onto the total buoyancy gradient vector (baroclinically low PV in Fig. 11). If this water parcel is then moved into the core of the TIV, where there is nonzero stratification and no horizontal buoyancy gradient, it must obtain anticyclonic vorticity of $-f$ in order to conserve PV (vertically low PV in Fig. 11). The ingredients required for this process are not only the source of baroclinically low PV in the EUC shear layer, but also a differential vertical circulation [$\partial w/\partial y$ and $\partial w/\partial x$ in Eq. (8)] that drives the vortex tilting. The western portion of the vortex in which this conversion process occurs is characterized by strong strain, as indicated by the straining of the example particle positions into a thin line between yeardays 283.4 and 285 (Fig. 8b), the same time period over which PV conversion and vortex tilting occurs (Fig. 9). Horizontal strain occurring in the presence of a horizontal buoyancy gradient can give rise to frontogenesis and a secondary circulation that provides the differential vertical motions required for the vortex tilting.

4. Frontogenesis

The particles considered in the previous section enter the vortex along a path that runs through the frontal regions in the western portion of the vortex. Both the trailing edge and leading edge fronts (Fig. 4) form as a result of frontogenesis. The equation governing the Lagrangian evolution of the horizontal buoyancy gradient in the absence of diabatic processes is

$$\frac{D|\nabla_h b|^2}{Dt} = \underbrace{-2\nabla_h b \cdot \left(\frac{\partial \mathbf{u}_h}{\partial x}\cdot\nabla_h b, \frac{\partial \mathbf{u}_h}{\partial y}\cdot\nabla_h b\right)}_{\text{HCL}} \underbrace{- 2\nabla_h b \cdot (N^2 \nabla_h w)}_{\text{DVADV}} . \tag{12}$$

The horizontal buoyancy gradient can change because of horizontal strain and shearing [HCL in Eq. (12)], differential vertical advection in a stratified fluid [DVADV in Eq. (12)] and diabatic processes that have been neglected. The western portion of the vortex around the LEF and TEF is characterized by strong positive HCL, indicating that the horizontal velocity field is increasing the horizontal buoyancy gradient here (Fig. 12). HCL reaches $\sim 10^{-17}\,\mathrm{s}^{-5}$, which is enough to increase $|\nabla_h b|$ by up to $\sim 10^{-6}\,\mathrm{s}^{-2}$ in 1 day.

According to the classical frontogenesis theories of Hoskins and Bretherton (1972) and Hoskins (1982), a front undergoing strain and shearing that acts to increase the horizontal buoyancy gradient (i.e., HCL > 0) will acquire an ageostrophic secondary circulation in the across-front plane in the sense to restore thermal wind balance by increasing the vertical shear in the geostrophic flow, reducing the horizontal buoyancy gradient and restratifying the front. These theories assume that thermal wind balance is a dominant constraint on the flow, which is part of the force balance along the TEF (Fig. 5). Thus,

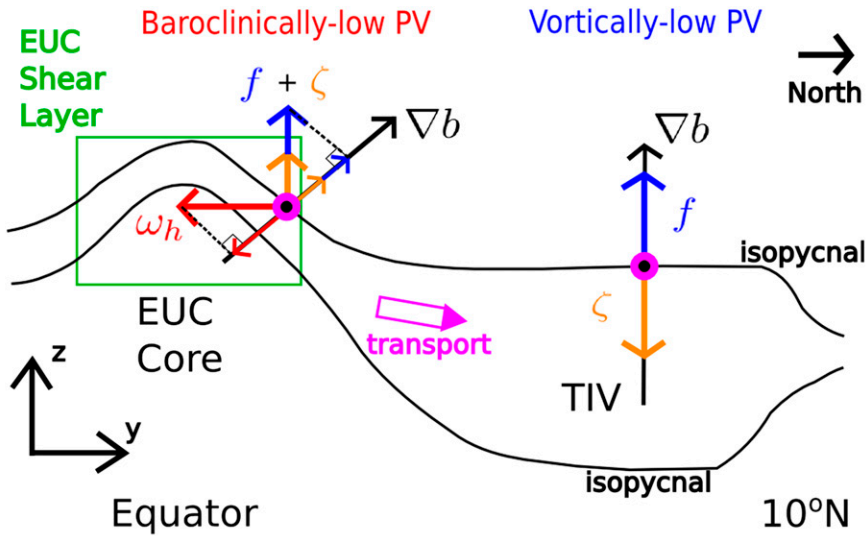

FIG. 11. A schematic showing the process of baroclinically low to vortically low PV conversion acting to form the strong anticyclonic rotation of a TIV. A parcel of water in the EUC shear layer (left pink circle) has baroclinically low PV as the projection of the horizontal vorticity onto the total buoyancy gradient vector compensates the projection of the vertical vorticity onto the total buoyancy gradient vector. If the parcel of water is moved into the TIV core (right pink circle), where the horizontal buoyancy gradient is small, then it must obtain strong anticyclonic rotation in order to conserve PV.

we may expect such a secondary circulation to be associated with the horizontal confluence/shearing in the western portion of the vortex.

The ageostrophic secondary circulation associated with frontogenesis is thermally direct in the sense that the buoyancy flux $w'b'$, where the prime denotes a deviation from an across-front average, is positive and acts to reduce the horizontal buoyancy gradient. Such a circulation will act to tilt the horizontal vorticity downward, providing that horizontal vorticity is ''anticyclonic'' (Molemaker et al. 2005), that is, it results in a negative value of the baroclinic PV, which is always the case for a flow in thermal wind balance. Therefore, the signature of an ageostrophic secondary circulation driven by frontogenesis is a frontal region with correlations between positive HCL, positive $w'b'$, and negative vortex tilting $\boldsymbol{\omega}_h \cdot \boldsymbol{\nabla}_h w$ [the third and fourth terms on the right-hand side of Eq. (8)].

The area of interest is along the TIV core water entrance pathway through the TIW cold cusp on the western side of the TIV. Here the cold cusp is experiencing strong strain and shearing as the LEF and TEF fronts are squeezed together (Figs. 4, 12) in a process resemblant of the filament intensification of McWilliams et al. (2009). A feature of this cold cusp is a near-surface filament of high PV associated with the cyclonic side of the LEF (marked with the green LEF line in Figs. 4, 13c). As a consequence of PV conservation, this near-surface, high-PV filament acts as a barrier to surface cross-flow and therefore separates the surface water to its northwest, outside the vortex, from surface water to its southeast, inside the vortex. Using this near-surface high-PV filament as a reference frame, we have calculated across-front slices of PV, vertical velocity, vortex tilting, $w'b'$, and HCL (Figs. 13a,b,d–f, respectively) averaged over the region indicated in Fig. 13c. The slices are calculated by performing an alongfront average within this region

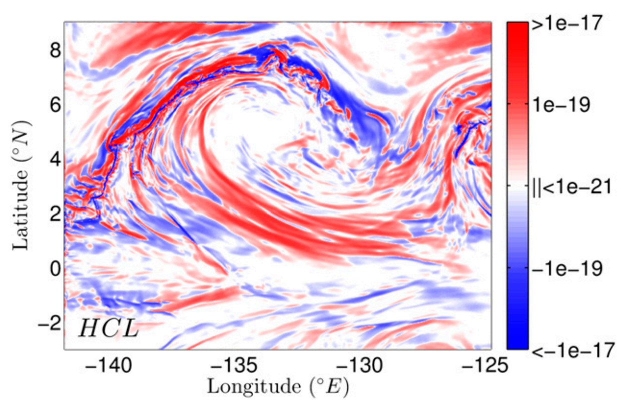

FIG. 12. The log of the horizontal strain and shearing term [HCL (s^{-5})] in the equation for the Lagrangian change in horizontal buoyancy gradient magnitude [Eq. (12)] at 50-m depth in the high-resolution simulation on 11 Oct (yearday 281.2083). Note that the color scale has been adjusted in order to show both frontogenetic and frontolytic values on a log scale.

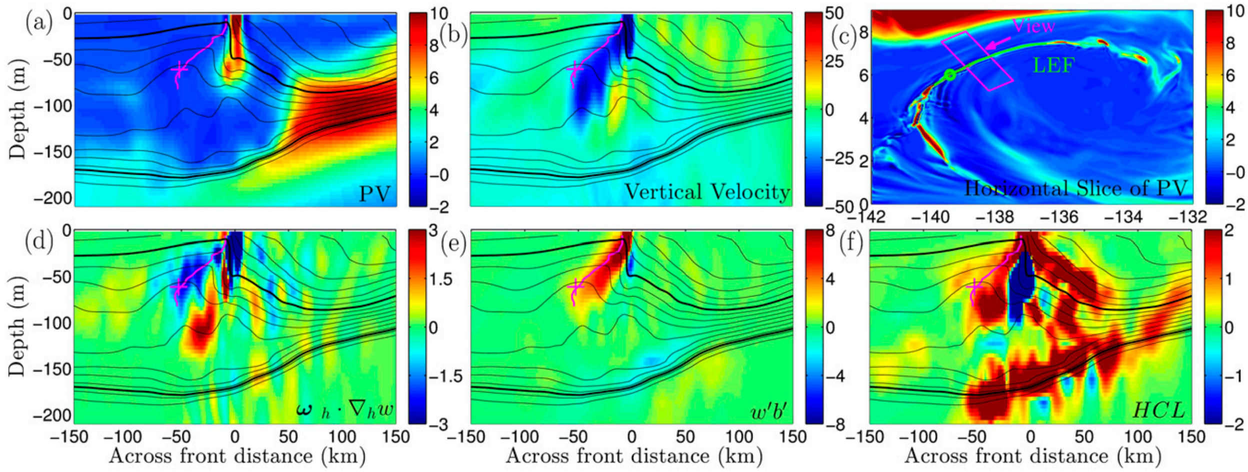

FIG. 13. Composite average across-front slices of (a) PV ($\times 10^{-9}\,\mathrm{s}^{-3}$), (b) vertical velocity ($\mathrm{m\,day}^{-1}$), (d) vortex tilting $\boldsymbol{\omega}_h \cdot \nabla_h w$ ($\times 10^{-10}\,\mathrm{s}^{-2}$), (e) buoyancy flux $w'b'$ ($\times 10^{-7}\,\mathrm{m}^2\,\mathrm{s}^{-3}$), and (f) HCL ($\times 10^{-19}\,\mathrm{s}^{-5}$) over 72 h from yearday 282.79 to yearday 285.63 (36 separate times) in the high-resolution simulation. (c) The region location is shown by the magenta box over a horizontal slice of the PV ($\times 10^{-9}\,\mathrm{s}^{-3}$) at 17-m depth halfway through the composite average time period (yearday 284.21). The reference point used for the time composite average is the intersection point of the near-surface, high-PV filament (green line marked LEF) with the 6° latitude line [shown with a green circle in (c)]. The composite average is performed by moving the region in time in order to keep its center point a constant zonal distance from this reference point. The angle of the region is maintained perpendicular to the LEF. The prime in the calculation of the buoyancy flux $w'b'$ in (e) is defined as the difference from a 75-km boxcar across-front filter at each depth. The result is robust for filter sizes between 25 and 125 km. HCL denotes changes in the horizontal buoyancy gradient driven by horizontal strain/shear [Eq. (12)]. The across-front position of the cold filament is marked by the magenta line, being the maximum in density at each depth. The average position of the 56 particles considered in the Lagrangian analysis in Figs. 8 and 9 relative to the LEF is shown by the magenta plus symbol. The thin black lines represent isopycnals with a spacing of 0.2 $\mathrm{kg\,m}^{-3}$ down to 1024.6 $\mathrm{kg\,m}^{-3}$, and the thick lines are the 1022.8 and 1024.3 $\mathrm{kg\,m}^{-3}$ isopycnals bounding the TIV control volume.

(magenta box in Fig. 13c) and a time composite average over a time period of 72 h (36 separate times) in order to show only the robust features.

The results show that the water surrounding the LEF moves downward as it moves rapidly northeast, with vertical velocities reaching up to 50 $\mathrm{m\,day}^{-1}$ (Fig. 13b). The strong positive HCL at the surface responsible for the formation and maintenance of the LEF is accompanied by strong negative HCL at middepths (Fig. 13f). This region of negative HCL is surrounded on either side by positive HCL. The across-front position of the maximum density at each depth, marking the peak of the TIW cold cusp, moves from 0 to -50 km toward the center of the vortex with depth (marked with the magenta line in Figs. 13a,b,d–f). It is through this cold filament that cold EUC water is entering the vortex. In particular, the set of 56 particles considered in the Lagrangian analysis (Figs. 8, 9) move through this cold filament (their average position is indicated by the magenta cross in Figs. 13a,b,d–f). This cold filament is characterized by positive HCL below depths of 25 m (Fig. 13f, around magenta line). The buoyancy flux around the cold filament is positive (Fig. 13e, around magenta line), indicating that the cold filament is experiencing a thermally direct circulation coincident with the positive HCL. Finally, this cold filament is also characterized by negative vortex tilting (Fig. 13d, around magenta line), and thus, there is strong evidence that the water in this cold filament is subject to a thermally direct secondary circulation associated with frontogenesis that acts to tilt horizontal vorticity downward. The composite average vortex tilting reaches magnitudes of $-2 \times 10^{-10}\,\mathrm{s}^{-2}$ (Fig. 13d), which is enough to reduce the relative vorticity by $-1.7 \times 10^{-5}\,\mathrm{s}^{-1}$ in 1 day, on the same order as that observed in the Lagrangian analysis (Fig. 9b).

5. Discussion

This work has focused on the vortex dynamics of fully developed TIVs, in contrast to many previous studies that considered the energetics of tropical instabilities. While these two different approaches generally tackle different questions, it is possible to make some broad connections between them. As described by Proehl (1996), tropical instabilities on a time-independent zonal flow can gain kinetic energy through lateral shear production (BT), vertical shear production (VS), and from background potential energy sources (BC):

$$\mathrm{BT} = -\overline{u'v'}\frac{\partial \overline{u}}{\partial y}, \tag{13}$$

$$\mathrm{VS} = -\overline{u'w'}\frac{\partial \overline{u}}{\partial z}, \quad \text{and} \tag{14}$$

$$\mathrm{BC} = \overline{w'b'}, \tag{15}$$

where the prime denotes a perturbation from a zonal average (indicated by the overbar). Using simple scaling arguments, it can be shown that the relative importance of the vertical to lateral shear production VS/BT is dependent on the relative size of the baroclinic term in the PV. To do this, we make a simple scaling assumption about the momentum fluxes associated with the tropical instabilities, namely, that the vertical momentum flux $\overline{u'w'}$ is an order one constant times the horizontal momentum flux $\overline{u'v'}$ times the isopycnal slope of the background flow:

$$\overline{u'w'} \sim -\frac{\partial \overline{b}/\partial y}{\overline{N^2}}\overline{u'v'}, \tag{16}$$

that is, we assume that the flow runs mostly along isopycnals. This scaling law was found to be qualitatively accurate in the TIV region by calculating perturbations from a zonal mean in the basinwide simulation. Under this scaling assumption, we find that the ratio of the vertical shear production to lateral shear production energy source terms for perturbation kinetic energy is controlled by the ratio of terms in the background PV:

$$\frac{\mathrm{VS}}{\mathrm{BT}} \sim \frac{q_h}{\zeta N^2}. \tag{17}$$

Thus, the large relative magnitude of the baroclinic PV component in the region above the EUC shear layer (Fig. 3) implies that vertical shear production may make a significant contribution to the kinetic energy of the tropical instabilities and hence to the vorticity of TIVs. Previous studies have concluded that this term is negligible (Weisberg and Weingartner 1988; Masina et al. 1999; Grodsky et al. 2005) or makes a small contribution (Cox 1980; Qiao and Weisberg 1998). It should be mentioned that the relative magnitude and sign of the different energy sources vary significantly with season and location (Luther and Johnson 1990; Masina et al. 1999) and with the level of lateral mixing included in the model (Pezzi and Richards 2003).

6. Conclusions

Using a set of nested high-resolution simulations of the equatorial Pacific, we have studied the vortex dynamics of TIVs making extensive use of the Ertel PV. This approach has yielded insights into TIV dynamics and revealed analogies between TIVs and submesoscale processes in the midlatitudes. The $O(1)$ Richardson numbers associated with the high vertical shear in the EUC shear layer (Fig. 2f) indicate that the baroclinic component of the PV is of comparable magnitude to the vertical component (Fig. 3). This baroclinic component acts as a source of anticyclonic vorticity for developed TIVs (Fig. 10) through the mechanism of baroclinically low to vortically low PV conversion (Fig. 11), a mechanism that is also involved in the formation of submesoscale intrathermocline eddies in the midlatitudes (Thomas 2008). However, in contrast to submesoscale flows at midlatitudes, the gradient in planetary vorticity plays an important role in the dynamics of TIVs. Specifically, a large fraction of the change in vertical relative vorticity experienced by water parcels entering a TIV is associated with a change in planetary vorticity. It is important to note, however, that our analysis of Lagrangian trajectories of TIV core water showed that very little of this low-PV water is sourced from the Southern Hemisphere (Fig. 7d). This is contrary to the results of Foltz et al. (2004), who found that some northward cross-hemisphere exchange occurred in the western Atlantic. Our simulations suggest that there is little evidence for significant northward cross-hemisphere exchange associated with TIVs in the central and eastern equatorial Pacific.

We have shown that vortex tilting of horizontal vorticity associated with the EUC shear layer provides a significant source for the anticyclonic rotation of the vortex (contributing −0.35 of a Rossby number on average, Fig. 10). This vortex tilting is consistent with a frontogenetic secondary circulation driven by the strain induced by the velocity field of the TIV itself. This work has highlighted the importance of frontal dynamics to the larger-scale circulation in the equatorial Pacific. These frontal dynamics are influenced by the curvature in TIV streamlines. The frontal region on the western side of TIVs was found to be in cyclogeostrophic balance with the centrifugal force playing an important role (Fig. 5). Indeed, a study of the horizontal vorticity balance along the TEF (not shown) indicates that the gradient–wind balance holds closely in the moving frame of the TIV, with the shear in the centrifugal force being the dominant term. Despite the large curvature, the sign of the baroclinic PV component was in most cases negative; indicating that the horizontal vorticity associated with these fronts was consistent with thermal wind balance (Fig. 3b). This indicates that a thermally direct secondary circulation driven by frontogenesis will tilt vorticity downward as observed (Fig. 13d). However, the details of frontogenesis and the associated secondary circulation in a flow with such high curvature are as yet unknown and will be the subject of further research.

Capturing the frontal dynamics and the process of baroclinically low to vortically low PV conversion in an ocean model requires accurate simulation of the EUC shear layer and the associated horizontal buoyancy gradient. The details of the flow in this region may depend on the horizontal resolution, vertical resolution, and vertical mixing parameterization included in the model. For example, the relative importance of the baroclinic contribution to vertical vorticity reduces going from our midresolution to our low-resolution simulation, that is, the ratio of the mean δ_{-q_h} to mean δ_{-f} in Fig. 10 reduces from 0.62 to 0.56 for an equivalent calculation on the same TIVs in the low-resolution simulation. While this is not a large numeric difference, this effect is expected to be systematic with reducing resolution as the grid aspect ratio reduces. This suggests that the PV conversion mechanism and submesoscale physics may be difficult to resolve in low-resolution simulations and that the vortex dynamics may be altered. Indeed, Marchesiello et al. (2011) showed, using a test for numerical convergence as measured by an invariance of the kinetic energy spectrum with resolution, that horizontal grid spacings of less than 10 km are required to capture the submesoscale physics of TIVs well. Thus, global circulation models with $\sim 1°$ horizontal resolution may not simulate TIV dynamics correctly, which may have implications for TIV-driven lateral stirring and vertical mixing and thus for the heat budget of the equatorial region.

This work has suggested that nonconservative processes associated with friction and diabatic changes in buoyancy may play an important role in the dynamics of TIVs, for example, the mixing and homogenization of temperature and salinity, and the lowering of PV, that occurs in the process of TIV core water formation (Figs. 7a,c,e). A net lowering of PV can be driven by surface cooling or frictional processes associated with wind stress. Surface cooling is unlikely at these low latitudes, suggesting that in this case frictional processes are responsible. In the case of ITEs in the midlatitudes, the source of baroclinically low PV can be an upward surface PV flux through wind-driven destruction of PV (Thomas 2008). Frictional reduction of PV by the easterly trade winds that blow down-front along the north equatorial front and drive equatorial upwelling may be a process of importance for TIV dynamics and may be the only explanation for net lowering of PV. Quantifying the role of nonconservative processes in the dynamics of the PV and other tracers is the subject of a follow-up study to this work.

Acknowledgments. This work was supported by the National Oceanic and Atmospheric Administration Grant NA06OAR4310058. The computations were performed at the Stanford Center for Computational Earth and Environmental Science. The offline particle calculations were performed using ROMS offline floats written by X. Capet.

REFERENCES

Capet, X., J. McWilliams, M. Molemaker, and A. Shchepetkin, 2008: Mesoscale to submesoscale transition in the California current system. Part II: Frontal processes. *J. Phys. Oceanogr.,* **38,** 44–64.

Cox, M. D., 1980: Generation and propagation of 30-day waves in a numerical model of the Pacific. *J. Phys. Oceanogr.,* **10,** 1168–1186.

De Szoeke, S., S.-P. Xie, T. Miyama, K. Richards, and R. Small, 2007: What maintains the SST front north of the eastern Pacific equatorial cold tongue? *J. Climate,* **20,** 2500–2514.

Dugan, J. P., R. P. Mied, P. C. Mignerey, and A. F. Schuetz, 1982: Compact, intrathermocline eddies in the Sargasso Sea. *J. Geophys. Res.,* **87** (C1), 385–393.

Dutrieux, P., C. Menkes, J. Vialard, P. Flament, and B. Blanke, 2008: Lagrangian study of tropical instability vortices in the Atlantic. *J. Phys. Oceanogr.,* **38,** 400–417.

Flament, P., S. Kennan, R. Knox, P. Niiler, and R. Bernstein, 1996: The three-dimensional structure of an upper ocean vortex in the tropical Pacific Ocean. *Nature,* **383,** 610–613.

Foltz, G. R., J. A. Carton, and E. P. Chassignet, 2004: Tropical instability vortices in the Atlantic Ocean. *J. Geophys. Res.,* **109,** C03029, doi:10.1029/2003JC001942.

Grodsky, S. A., J. A. Carton, C. Provost, J. Servain, J. A. Lorenzzetti, and M. J. McPhaden, 2005: Tropical instability waves at 0°N, 23°W in the Atlantic: A case study using Pilot Research Moored Array in the Tropical Atlantic (PIRATA) mooring data. *J. Geophys. Res.,* **110,** C08010, doi:10.1029/2005JC002941.

Hansen, D. V., and C. A. Paul, 1984: Genesis and effects of long waves in the equatorial pacific. *J. Geophys. Res.,* **89** (C6), 10 431–10 440.

Hoskins, B., 1982: The mathematical theory of frontogenesis. *Annu. Rev. Fluid Mech.,* **14,** 131–151.

——, and F. Bretherton, 1972: Atmospheric frontogenesis models: Mathematical formulation and solution. *J. Atmos. Sci.,* **29,** 11–37.

Inoue, R., R. Lien, and J. Moum, 2012: Modulation of equatorial turbulence by a tropical instability wave. *J. Geophys. Res.,* **117,** C10009, doi:10.1029/2011JC007767.

Jochum, M., P. Malanotte-Rizzoli, and A. Busalacchi, 2004: Tropical instability waves in the Atlantic Ocean. *Ocean Modell.,* **7,** 145–163.

Johnson, E. S., 1996: A convergent instability wave front in the central tropical Pacific. *Deep-Sea Res. II,* **43,** 753–778.

——, and J. A. Proehl, 2004: Tropical instability wave variability in the Pacific and its relation to large-scale currents. *J. Phys. Oceanogr.,* **34,** 2121–2147.

Johnson, G., and M. McPhaden, 2001: Equatorial Pacific Ocean horizontal velocity, divergence, and upwelling. *J. Phys. Oceanogr.,* **31,** 839–849.

Kennan, S., and P. Flament, 2000: Observations of a tropical instability vortex. *J. Phys. Oceanogr.,* **30,** 2277–2301.

Kostianoy, A., and I. Belkin, 1989: A survey of observations on emtrathermocline eddies in the world ocean. *Mesoscale/ Synoptic Coherent Structures in Geophysical Turbulence,* J. Nihoul and B. Jamart, Eds., Elsevier Oceanography Series, Vol. 50, Elsevier, 821–841.

Large, W. G., and S. G. Yeager, 2004: Diurnal to decadal global forcing for ocean and sea-ice models: The data sets and flux climatologies. NCAR Tech. Note NCAR/TN-460+STR, 105 pp. [Available online at http://nldr.library.ucar.edu/repository/assets/technotes/TECH-NOTE-000-000-000-601.pdf.]

——, J. C. McWilliams, and S. C. Doney, 1994: Oceanic vertical mixing: A review and a model with a nonlocal boundary layer parameterization. *Rev. Geophys.,* **32,** 363–404.

Legeckis, R., 1977: Long waves in the eastern equatorial Pacific Ocean: A view from a geostationary satellite. *Science,* **197,** 1179–1181.

Lien, R.-C., E. A. D'Asaro, and C. E. Menkes, 2008: Modulation of equatorial turbulence by tropical instability waves. *Geophys. Res. Lett.,* **35,** L24607, doi:10.1029/2008GL035860.

Luther, D. S., and E. S. Johnson, 1990: Eddy energetics in the upper equatorial pacific during the Hawaii-to-Tahiti shuttle experiment. *J. Phys. Oceanogr.,* **20,** 913–944.

Lyman, J. B., G. Johnson, and W. Kessler, 2007: Distinct 17- and 33-day tropical instability waves in subsurface observations. *J. Phys. Oceanogr.,* **37,** 855–872.

Marchesiello, P., X. Capet, C. Menkes, and S. Kennan, 2011: Submesoscale dynamics in tropical instability waves. *Ocean Modell.,* **39,** 31–46.

Masina, S., S. G. H. Philander, and A. B. G. Bush, 1999: An analysis of tropical instability waves in a numerical model of the Pacific Ocean: 2. Generation and energetics of the waves. *J. Geophys. Res.,* **104** (C12), 29 637–29 661.

McWilliams, J. C., 1985: Submesoscale, coherent vortices in the ocean. *Rev. Geophys.,* **23,** 165–182.

——, F. Colas, and M. J. Molemaker, 2009: Cold filamentary intensification and oceanic surface convergence lines. *Geophys. Res. Lett.,* **36,** L18602, doi:10.1029/2009GL039402.

Menkes, C., J. Vialard, S. Kennan, J. Boulanger, and G. Madec, 2006: A modeling study of the impact of tropical instability waves on the heat budget of the eastern equatorial Pacific. *J. Phys. Oceanogr.,* **36,** 847–865.

Molemaker, M., J. McWilliams, and I. Yavneh, 2005: Baroclinic instability and loss of balance. *J. Phys. Oceanogr.,* **35,** 1505–1517.

Moum, J. N., R.-C. Lien, A. Perlin, J. Nash, M. Gregg, and P. Wiles, 2009: Sea surface cooling at the equator by subsurface mixing in tropical instability waves. *Nat. Geosci.,* **2,** 761–765.

——, A. Perlin, J. D. Nash, and M. J. McPhaden, 2013: Seasonal sea surface cooling in the equatorial Pacific cold tongue controlled by ocean mixing. *Nature,* **500,** 64–67.

Pezzi, L. P., and K. J. Richards, 2003: Effects of lateral mixing on the mean state and eddy activity of an equatorial ocean. *J. Geophys. Res.,* **108,** 3371, doi:10.1029/2003JC001834.

Philander, S. G. H., 1976: Instabilities of zonal equatorial currents. *J. Geophys. Res.,* **81,** 3725–3735.

——, 1978: Instabilities of zonal equatorial currents, 2. *J. Geophys. Res.,* **83** (C7), 3679–3682.

Proehl, J. A., 1996: Linear stability of equatorial zonal flows. *J. Phys. Oceanogr.,* **26,** 601–621.

Qiao, L., and R. H. Weisberg, 1995: Tropical instability wave kinematics: Observations from the tropical instability wave experiment. *J. Geophys. Res.,* **100** (C5), 8677–8693.

——, and ——, 1998: Tropical instability wave energetics: Observations from the tropical instability wave experiment. *J. Phys. Oceanogr.,* **28,** 345–360.

Shchepetkin, A., and J. McWilliams, 2005: The Regional Oceanic Modeling System (ROMS): A split-explicit, free-surface, topography-following-coordinate oceanic model. *Ocean Modell.,* **9,** 347–404.

Spall, M., 1995: Frontogenesis, subduction, and cross-front exchange at upper ocean fronts. *J. Geophys. Res.,* **100** (C2), 2543–2557.

Thomas, L. N., 2005: Destruction of potential vorticity by winds. *J. Phys. Oceanogr.,* **35,** 2457–2466.

——, 2008: Formation of intrathermocline eddies at ocean fronts by wind-driven destruction of potential vorticity. *Dyn. Atmos. Oceans,* **45,** 252–273.

——, A. Tandon, and A. Mahadevan, 2008: Submesoscale processes and dynamics. *Ocean Modeling in an Eddying Regime, Geophys. Monogr.,* Vol. 177, Amer. Geophys. Union, 17–38.

Ubelmann, C., and L.-L. Fu, 2011: Cyclonic eddies formed at the Pacific tropical instability wave fronts. *J. Geophys. Res.,* **116,** C12021, doi:10.1029/2011JC007204.

Vialard, J., C. Menkes, J.-P. Boulanger, P. Delecluse, E. Guilyardi, M. J. McPhaden, and G. Madec, 2001: A model study of oceanic mechanisms affecting equatorial Pacific sea surface temperature during the 1997–98 El Niño. *J. Phys. Oceanogr.,* **31,** 1649–1675.

Weisberg, R. H., and T. J. Weingartner, 1988: Instability waves in the equatorial Atlantic Ocean. *J. Phys. Oceanogr.,* **18,** 1641–1657.

Willett, C. S., R. R. Leben, and M. F. Lavn, 2006: Eddies and tropical instability waves in the eastern tropical Pacific: A review. *Prog. Oceanogr.,* **69,** 218–238.

Yu, J., and W. Liu, 2003: A linear relationship between enso intensity and tropical instability wave activity in the eastern Pacific Ocean. *Geophys. Res. Lett.,* **30,** 1735, doi:10.1029/2003GL017176.

Yu, Z., J. P. McCreary, and J. A. Proehl, 1995: Meridional asymmetry and energetics of tropical instability waves. *J. Phys. Oceanogr.,* **25,** 2997–3007.